Chemistry & Biochemistry Faculty Publications   Chemistry & Biochemistry

2024

Opacities of S-type Stars: The Singlet B¹Π–X¹Σ⁺, B¹Π–A¹Δ, and C¹Σ⁺–X¹Σ⁺ Band Systems of ZrO

Peter F. Bernath
Old Dominion University, pbernath@odu.edu

Manish Bhusal
Old Dominion University, mbhus001@odu.edu

Jacques Liévin
Université Libre de Bruxelles

Opacities of S-type Stars: The Singlet $B^1\Pi$–$X^1\Sigma^+$, $B^1\Pi$–$A^1\Delta$, and $C^1\Sigma^+$–$X^1\Sigma^+$ Band Systems of ZrO

Peter F. Bernath[1,2] , Manish Bhusal[2] , and Jacques Liévin[3]
[1] Department of Chemistry and Biochemistry, Old Dominion University, Norfolk, VA 23529, USA
[2] Department of Physics, Old Dominion University, Norfolk, VA 23529, USA
[3] Université Libre de Bruxelles, Spectroscopy, Quantum Chemistry and Atmospheric Remote Sensing, CP 160/09, Av. F. D. Roosevelt 50, Bruxelles, Belgium; mbhus001@odu.edu

Abstract

The ZrO $B^1\Pi$–$X^1\Sigma^+$, $B^1\Pi$–$A^1\Delta$, and $C^1\Sigma^+$–$X^1\Sigma^+$ band systems are important opacity sources in the near-infrared and optical spectra of S-type stars. A total of 21 rovibronic bands with $v'' \leqslant 7$ and $v' \leqslant 5$ were observed and fit for the $B^1\Pi$–$X^1\Sigma^+$ transition, five bands for the ^{90}ZrO $B^1\Pi$–$A^1\Delta$ transition and one band for the ^{90}ZrO $C^1\Sigma^+$–$X^1\Sigma^+$ transition. All band systems were analyzed using high-temperature, high-resolution emission spectra collected at the National Solar Observatory (Kitt Peak). A modern spectroscopic analysis was performed using the PGOPHER program to provide updated spectroscopic constants. In general, we improve the accuracy of the line positions reported in the literature and slightly extend the vibrational analysis. Equilibrium molecular constants were then derived and combined with new ab initio calculations of transition dipole moment functions to produce line lists with line strengths.

Unified Astronomy Thesaurus concepts: Spectral line lists (2082); Molecular spectroscopic constants (2260); Rotational spectroscopy (2248)

Supporting material: data behind figure, machine-readable tables

1. Introduction

The presence of ZrO bands are characteristic features of S-type stars. Merrill (1922) identified the S class of stars as distinct from M stars (characterized by TiO bands) and carbon stars (C type, with C_2 bands). S stars (Merrill 1922) have a number of unique absorption features that were not assigned to a particular carrier. The following year Merrill (1923) recorded the spectrum of a Zr arc in air and by direct comparison with the red spectra of S-type stars (R Cygni and others) assigned these features to ZrO. The extensive analysis of ZrO laboratory spectra began in the 1930s with the work of Lowater (1932, 1935).

S stars are red giant and asymptotic giant branch (AGB) stars that are part of the M-MS-S-SC-C stellar sequence determined by increasing carbon abundance (Keenan 1954; Ake 1979; Keenan & Boeshaar 1980). As stars leave the main sequence, He burning increases the C/O abundance ratio from less than 1 for M stars to greater than 1 for C stars. S stars have C/O abundance ratios of about 1. Zr is produced in the s-process by neutron capture and subsequent β decay. The classification of S-type stars is based primarily on the strength of ZrO bands (Keenan 1954; Ake 1979; Keenan & Boeshaar 1980).

Merrill (1952) discovered technetium (Tc) lines in the spectra of S-type stars. There are no stable Tc isotopes, and ^{99}Tc has a half-life of 2.1×10^5 yr in the laboratory. Only ^{99}Tc is produced by the s-process in AGB stars (Van Eck & Jorissen 1999). There are two types of S stars: intrinsic S stars contain Tc and extrinsic S stars do not. Extrinsic S stars are binaries in which the s-process elements such as Zr were transferred from companion stars (Van Eck & Jorissen 2000). Zr isotope ratios provide information on the neutron density during the s-process (Lambert et al. 1995).

Owing to its astrophysical importance, ZrO has been extensively studied in the laboratory. As a transition metal oxide, ZrO has many low-lying electronic states, which lead to numerous optical and near-infrared transitions as illustrated by Figure 1 in the review paper by McKemmish et al. (2018). McKemmish et al. (2018) carried out a Measured Active Rotational-Vibrational Energy Levels (MARVEL) analysis that provided rovibronic energy levels from the observed line positions. In our present work, we focus on the band systems between the low-lying singlet states: $B^1\Pi$–$X^1\Sigma^+$, $B^1\Pi$–$A^1\Delta$, and $C^1\Sigma^+$–$X^1\Sigma^+$. Very recently (after the submission of this manuscript), Perri et al. (2023) published an extensive new line list and partition function for ZrO.

The first rotational analysis of the 0–0 band of the $B^1\Pi$–$X^1\Sigma^+$ transition for ^{90}Zr^{16}O, ^{94}Zr^{16}O, and ^{96}Zr^{16}O was performed by Balfour & Tatum (1973). They analyzed ZrO emission spectra recorded with a spectrograph by S. Davis and coworkers at the University of California, Berkeley using an arc source from ZrO_2 in natural abundance and three isotopically enriched samples (Tatum & Balfour 1973). Later, Phillips & Davis (1976a) analyzed many additional ZrO $B^1\Pi$–$X^1\Sigma^+$ bands using the same photographic plates. Pettersson et al. (2000) measured the $B^1\Pi$-state dipole moment to be 3.43 D. More recently, we carried out an analysis of 13 ^{90}Zr^{16}O $B^1\Pi$–$X^1\Sigma^+$ bands with vibrational levels up to four in both ground and excited states using carbon furnace emission spectra recorded with the National Solar Observatory Fourier transform spectrometer (Sorensen & Bernath 2021).

The 0–0 band of the $C^1\Sigma^+$–$X^1\Sigma^+$ transition was first observed by Phillips & Davis (1976b) for ^{90}Zr^{16}O, ^{94}Zr^{16}O, and ^{96}Zr^{16}O utilizing a zirconium arc source and the photographic plates cited above. The 0–0 band was later analyzed by Simard et al. (1988)

for ^{90}Zr^{16}O, ^{91}Zr^{16}O, ^{92}Zr^{16}O, ^{94}Zr^{16}O, and ^{96}Zr^{16}O using laser-induced fluorescence of a supersonically cooled ZrO molecular beam. Zr has five naturally occurring isotopes with abundances ^{90}Zr 51.5%, ^{91}Zr 11.2%, ^{92}Zr 17.2%, ^{94}Zr 17.4%, and ^{96}Zr 2.8% (Rumble 2022). Simard et al. (1988) also measured the radiative lifetimes of several vibrational levels of the $C^1\Sigma^+$ and $B^1\Pi$ states. Balfour & Chowdhury (2010) have reported the 0–0, 1–1, 1–0, 2–2, 3–3, 2–0, and 3–0 R-band heads for the $C^1\Sigma^+$–$X^1\Sigma^+$ transition.

For the $B^1\Pi$–$A^1\Delta$ transition, Hammer & Davis (1981) used a carbon furnace and a Fourier transform spectrometer (FTS) to report line positions of the 0–0, 0–1, 1–0, 1–1, and 2–1 bands of ^{90}Zr^{16}O and the 0–0 bands for ^{91}Zr^{16}O, ^{92}Zr^{16}O, ^{94}Zr^{16}O, and ^{96}Zr^{16}O (Hammer & Davis 1981; Hammer et al. 1981).

There have been two microwave studies of ZrO, the first of which was performed by Suenram et al. (1990) in which the $X^1\Sigma^+$ $J = 1$–0 transition frequencies for $v = 0$ for ^{91}Zr^{16}O, ^{92}Zr^{16}O, and ^{94}Zr^{16}O were measured using a laser ablation source coupled with a Fourier transform microwave spectrometer. They also measured the $X^1\Sigma^+$ ZrO dipole moment to be 2.55 D. The second study by Beaton & Gerry (1999) extended Suenram et al. (1990)'s work to provide the $X^1\Sigma^+$ $J = 1$–0 transition frequencies for excited vibrational levels and for additional isotopologues.

Additional experimental observations include the anion photoelectron spectrum of ZrO$^-$, which yields a ZrO electron affinity of 1.26 eV (Li et al. 2012). The photoelectron spectrum of ZrO gives an ionization energy of 6.8127 eV (Luo et al. 2015). The ZrO dissociation energy D° is 7.89 ± 0.15 eV (Murad & Hildenbrand 1975).

There have been several relevant theoretical calculations of ZrO properties. Langhoff & Bauschlicher (1988) carried out ab initio calculations of the spectroscopic constants of the low-lying electronic states. In 1990, they extended their work to include transition dipole moments and radiative lifetimes. Tabet et al. (2019) calculated spectroscopic properties, dipole moments, and transition dipole moments associated with a large number of ZrO singlet and triplet states. The recent paper by Perri et al. (2023) also carried out extensive ab initio calculations at a similar level of theory as that in Tabet et al. (2019).

This present paper is an extension of our previous work on ZrO (Sorensen & Bernath 2021) and improves on it in a number of ways. First, we extend the analysis of the observed ^{90}Zr^{16}O $B^1\Pi$–$X^1\Sigma^+$ bands and recalculate the line strengths with a new transition dipole moment. Second, we perform a PGOPHER spectroscopic analysis of the ^{90}Zr^{16}O $B^1\Pi$–$A^1\Delta$ (0–0, 0–1, 1–0, 1–1, and 2–1 bands) and $C^1\Sigma^+$–$X^1\Sigma^+$ (0–0 band) transitions. Third, we perform ab initio calculations reporting updated transition dipole moment functions for the $B^1\Pi$–$X^1\Sigma^+$, $B^1\Pi$–$A^1\Delta$, and $C^1\Sigma^+$–$X^1\Sigma^+$ transitions and use these data along with RKR potential energy curves to report line strengths.

2. Experiment

The ZrO emission spectra used in our work were recorded by S. Davis and coworkers using a carbon tube furnace (King furnace) in 1980 with the McMath–Pierce 1 m FTS at the National Solar Observatory at Kitt Peak in Arizona. For the $B^1\Pi$–$X^1\Sigma^+$ and $C^1\Sigma^+$–$X^1\Sigma^+$ transitions, ZrO$_2$ was heated to 2678 K with 72 Torr of He buffer gas. The ZrO thermal emission was measured with the Kitt Peak FTS using a visible

beamsplitter at a spectral resolution of 0.046 cm^{-1}. The spectral range 8400–24,000 cm^{-1} was set by a GG400 red pass filter (approximately 400 nm) and a silicon photodiode detector. Spectral calibration was carried out using Zr atomic lines (Lawler et al. 2022) with the linear equation $\sigma_{\rm cal} = 0.999997678\sigma_{\rm obs} + 0.0157$. The wavenumber scale was calibrated to better than 0.001 cm^{-1}. This spectrum had a slightly improved signal-to-noise ratio (S/N) and improved calibration compared to our previous work (Sorensen & Bernath 2021).

In the analysis of the $B^1\Pi$–$A^1\Delta$ transition, the spectrum described above was used for many of the lines. However, three additional Kitt Peak spectra recorded with similar experimental conditions were also used. Most of the 0–0 and 1–1 band lines were from a spectrum recorded at a temperature of 2663 K and a pressure of 68 Torr He. The spectral bandpass of 9000–9700 cm^{-1} was set with filters and the spectral resolution was 0.015 cm^{-1}. Calibration was carried out by comparison with the calibrated spectrum discussed above. The 9000–9700 cm^{-1} spectrum was shifted by -0.0328 cm^{-1} obtained using Zr atomic lines common to both spectra.

The $B^1\Pi$–$A^1\Delta$ 1–0 band region was partly analyzed with a spectrum covering 10,200–10,400 cm^{-1} at a spectral resolution of 0.025 cm^{-1}. The spectral range was set with a bandpass filter. The experimental conditions were 2673 K for temperature and 95 Torr of He buffer gas. The calibration again used Zr atomic lines and the spectrum was shifted by -0.0355 cm^{-1}.

The $B^1\Pi$–$A^1\Delta$ 0–1 band region was analyzed partly with a spectrum covering the 8200–8800 cm^{-1} region set by a bandpass filter at a spectral resolution of 0.025 cm^{-1}. The experimental conditions were 2723 K for temperature and 100 Torr of He buffer gas. The calibration again used Zr atomic lines and the wavenumber scale was multiplied by 0.999996829.

3. Ab Initio Calculations

The potential energy curves of the $X^1\Sigma^+$, $A^1\Delta$, $B^1\Pi$, and $C^1\Sigma^+$ states and the electric transition dipole moment curves for the $B^1\Pi$–$X^1\Sigma^+$, $B^1\Pi$–$A^1\Delta$, and $C^1\Sigma^+$–$X^1\Sigma^+$ transitions have been calculated with the MOLPRO quantum chemistry package (Werner et al. 2012, 2022) using the internally contracted multireference configuration interaction method (MRCI; Werner & Knowles 1988). State-averaged complete active space self-consistent field calculations (CASSCF; Werner & Knowles 1985; Kreplin et al. 2019) were performed to optimize the molecular orbitals (MOs) used in the MRCI calculations. Davidson's correction for unlinked quadruple excitations (Langhoff & Davidson 1974) adapted to a relaxed reference (Werner et al. 2008), has been taken into account in the energy calculations (MRCI+Q).

The 28 core electrons of the zirconium atom (Ar + 3d^{10}) are described by a small-core scalar-relativistic pseudo potential adjusted in multiconfiguration Dirac–Hartree–Fock calculations, and the remaining electrons are explicitly represented by the related cc-pwCVQZ-PP basis set (Peterson et al. 2007). The cc-pCVQZ basis set has been adopted for the oxygen atom (Woon & Dunning 1993). The active space defining the multiconfigurational reference wave functions contains five σ, three π, and one δ MOs correlating to the zirconium 5s, 4d, and oxygen 2s, 2p atomic orbitals, with an additional π orbital improving the correlation of oxygen 2pπ and zirconium 4dπ, as previously suggested (Langhoff & Bauschlicher 1990).
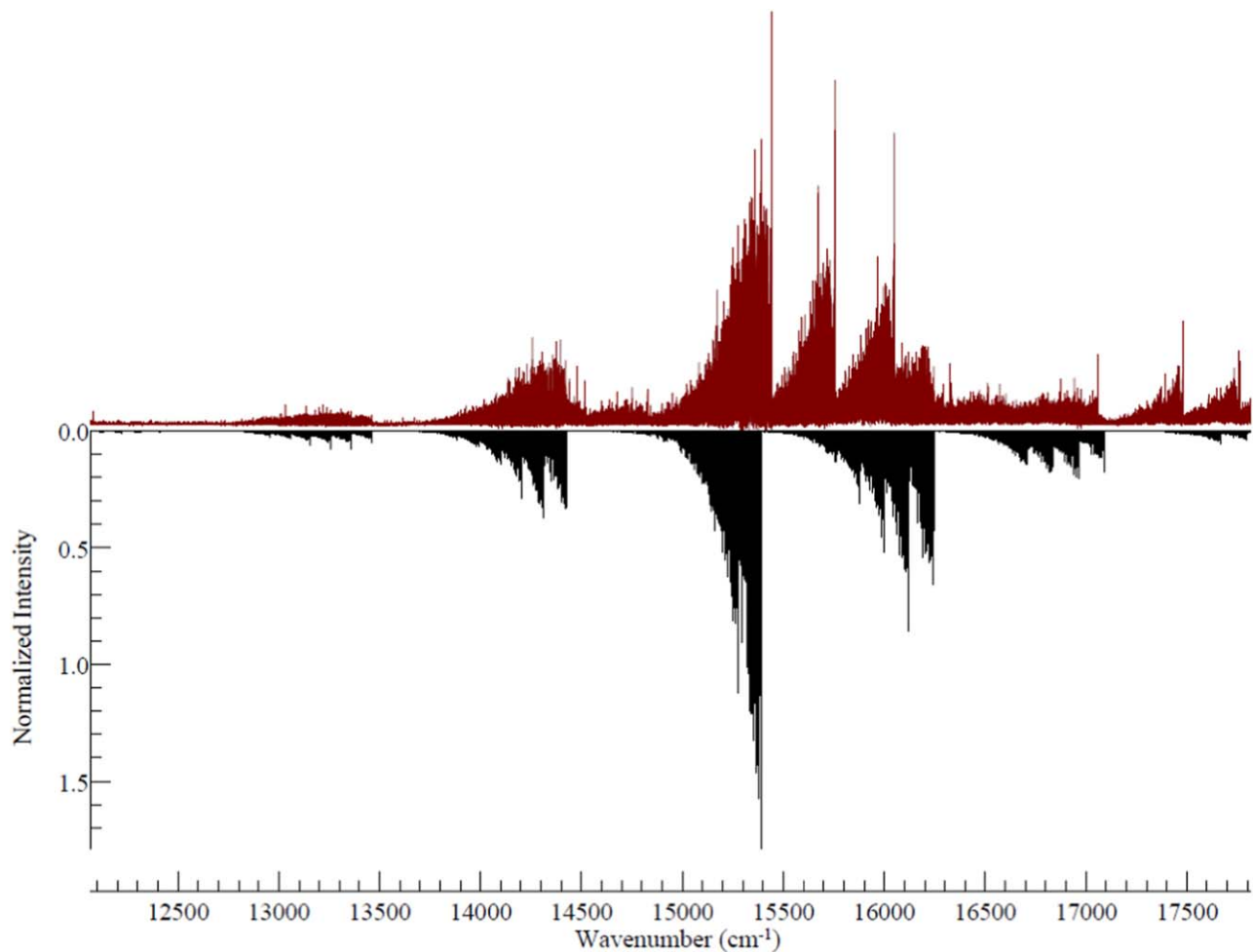
Figure 1. An overview of the spectrum for ZrO (red, upward) along with the simulated spectrum (black, downward) for 21 bands of the $^{90}\mathrm{Zr}^{16}\mathrm{O}$ $B^1\Pi–X^1\Sigma^+$ transition. Note that spectral features that are not simulated are largely associated with the $d^3\Phi–a^3\Delta$ transition, which will be discussed in a future publication.

Additional MOs (two σ and one π) correlating to the zirconium 4s and 4p orbitals have been included in the single and double excitations MRCI process, leading to the correlation of all 12 out-of-core electrons of zirconium. Only the 1s-like orbital of oxygen, which lies too deep for interacting appreciably with the valence shells, has been kept frozen. In order to reduce the large size of the resulting MRCI Hamiltonian matrix, we have selected the reference configurations from the CASSCF wave function using a threshold of 0.0001 for the CI coefficients. This resulted in MRCI expansions of some 160 million contracted configuration state functions. The analysis of these wave functions at equilibrium geometry provides for each calculated state the main contributing configurations with their weights of

$$X^1\Sigma^+ = 75\% \quad (A) \; + \; 6\% \quad (B) \; + \; 6\% \quad (C)$$
$$A^1\Delta = 79\% \quad (D) \; + \; 5\% \quad (C)$$
$$B^1\Pi = 54\% \quad (E) \; + \; 30\% \quad (F)$$
$$C^1\Sigma^+ = 77\% \quad (B) \; + \; 6\% \quad (A),$$

in which (A) is the ground configuration [core] $(1–5)\sigma^2 \, 1\pi^4 \, 2\pi^4$, and (B)–(F) correspond to the following electron promotions with respect to (A): $5\sigma^2 \rightarrow 1\delta^2$, $5\sigma^2 \rightarrow 3\pi^2$, $5\sigma^1 \rightarrow 1\delta^1$, $5\sigma^2 \rightarrow 1\delta^1 3\pi^1$, and $5\sigma^1 \rightarrow 3\pi^1$, respectively.

A balanced description of the states involved in the different transitions has been obtained by applying a CASSCF state averaging including the X, A and B states for the B–X and B–A transitions, while for the C–X transition it has proven important to include the X, A, and C states, but also the $D^1\Gamma$ and $C^3\Sigma^-$ states, arising as the C state from configuration (B).

The calculations have been carried out at a set of internuclear distances, r, ranging from 1.5–2.1 Å, in steps of 0.02 Å, providing the potential energy functions for the X, A, B, and C states and the transition dipole moment functions for the transitions of interest. The equilibrium spectroscopic properties for each state have been derived from Dunham 8th-order polynomial fits of the corresponding potential energy curves. The transition dipole moment functions have been interpolated by B-splines to create a set of 1592 points on the same r range, to be used in the determination of the band strengths. The calculated points and the interpolated points are provided as supplementary data. The ab initio results are presented and commented on in the discussion section.

4. Results

Spectral fitting was performed using the PGOPHER program (Western 2017). In the case of the $^{90}\mathrm{Zr}^{16}\mathrm{O}$ $B^1\Pi–X^1\Sigma^+$ transition, the spectroscopic constants from our previous study
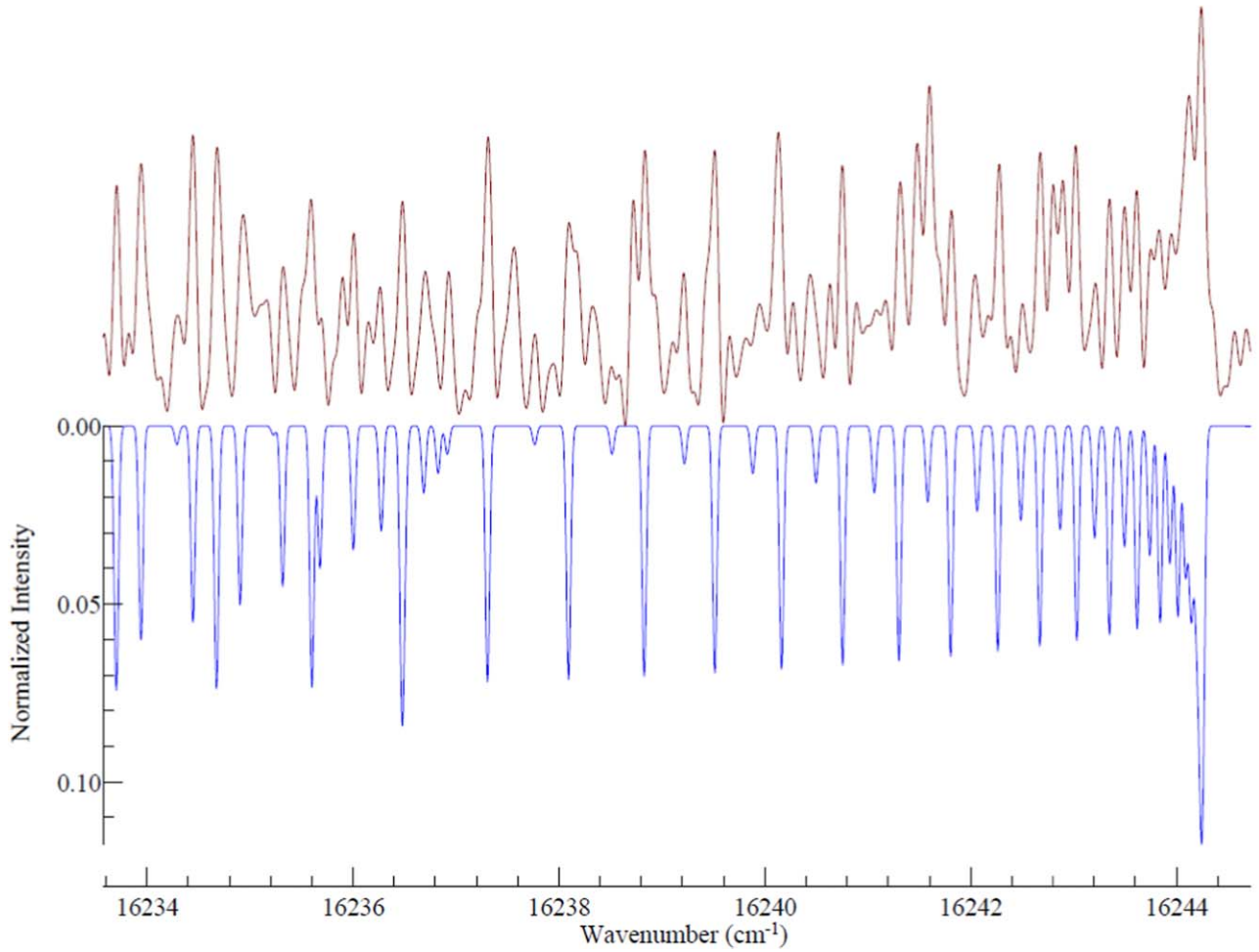
Figure 2. Typical $^{90}Zr^{16}O$ $B^1\Pi$–$X^1\Sigma^+$ spectrum (red, upward) with a simulated R-branch head for the 1–0 band (blue, downward).

Table 1
Calculated R-band Heads (in cm^{-1}) for the $^{90}Zr^{16}O$ $B^1\Pi$–$X^1\Sigma^+$ Transition

v'/v''	0	1	2	3	4	5	6	7
0	15,391.406	14,422.643	13,460.945	⋯	⋯	⋯	⋯	⋯
1	16,244.260	⋯	14,313.493	13,358.676	⋯	⋯	⋯	⋯
2	17,091.317	16,122.319	⋯	14,205.326	13,257.399	**12,316.624**	⋯	⋯
3	⋯	16,963.411	⋯	⋯	14,098.081	13,157.055	12,223.201	⋯
4	⋯	⋯	16,836.428	⋯	⋯	13,991.766	13057.662	**12,130.713**
5	⋯	⋯	⋯	16,710.295	⋯	⋯	⋯	12,959.137

Note. Plain text denotes R-band heads that have been previously reported. Bold text shows bands that are new.

were used as initial parameters (Sorensen & Bernath 2021). The ground $X^1\Sigma^+$ state was constrained by adding microwave data of the $J = 1–0$ transition for $v = 0, 1, 2,$ and 3 for $^{90}Zr^{16}O$ taken from Beaton & Gerry (1999)'s work. PGOPHER's default standard deviation of 1 was used for all fitted lines except for the microwave lines, which had their standard deviation weightings switched to 0.02.

An overview of the spectrum analyzed for the $B^1\Pi$–$X^1\Sigma^+$ transition (red, upward) is presented in Figure 1 along with a simulated spectrum (black, downward). A representative band head for each of the $B^1\Pi$–$X^1\Sigma^+$, $B^1\Pi$–$A^1\Delta$, and $C^1\Sigma^+$–$X^1\Sigma^+$ transitions is shown in Figures 2–4 along with their PGOPHER simulations. The additional weak features not simulated in these figures are due to Zr isotopologues and triplet transitions.

The spectra analyzed had a high spectral line density that made analysis difficult especially for higher vibrational levels. However, we were able to consistently assign transitions with J values in excess of 100, often in the 120–150 range.

As depicted in the ZrO energy diagram (Figure 1 in the paper by McKemmish et al. 2018), there are a large number of low-lying electronic states and many band systems falling in the visible and near-infrared spectral region. In our paper, we focus on the singlet systems, but the triplet systems (particularly α, β, γ) are equally significant and are mainly responsible for the missing features in the simulation shown in Figure 1.

In the case of the $B^1\Pi$–$X^1\Sigma^+$ transition, our fit contains a total of 5514 lines associated with 21 bands of $^{90}Zr^{16}O$, with an average
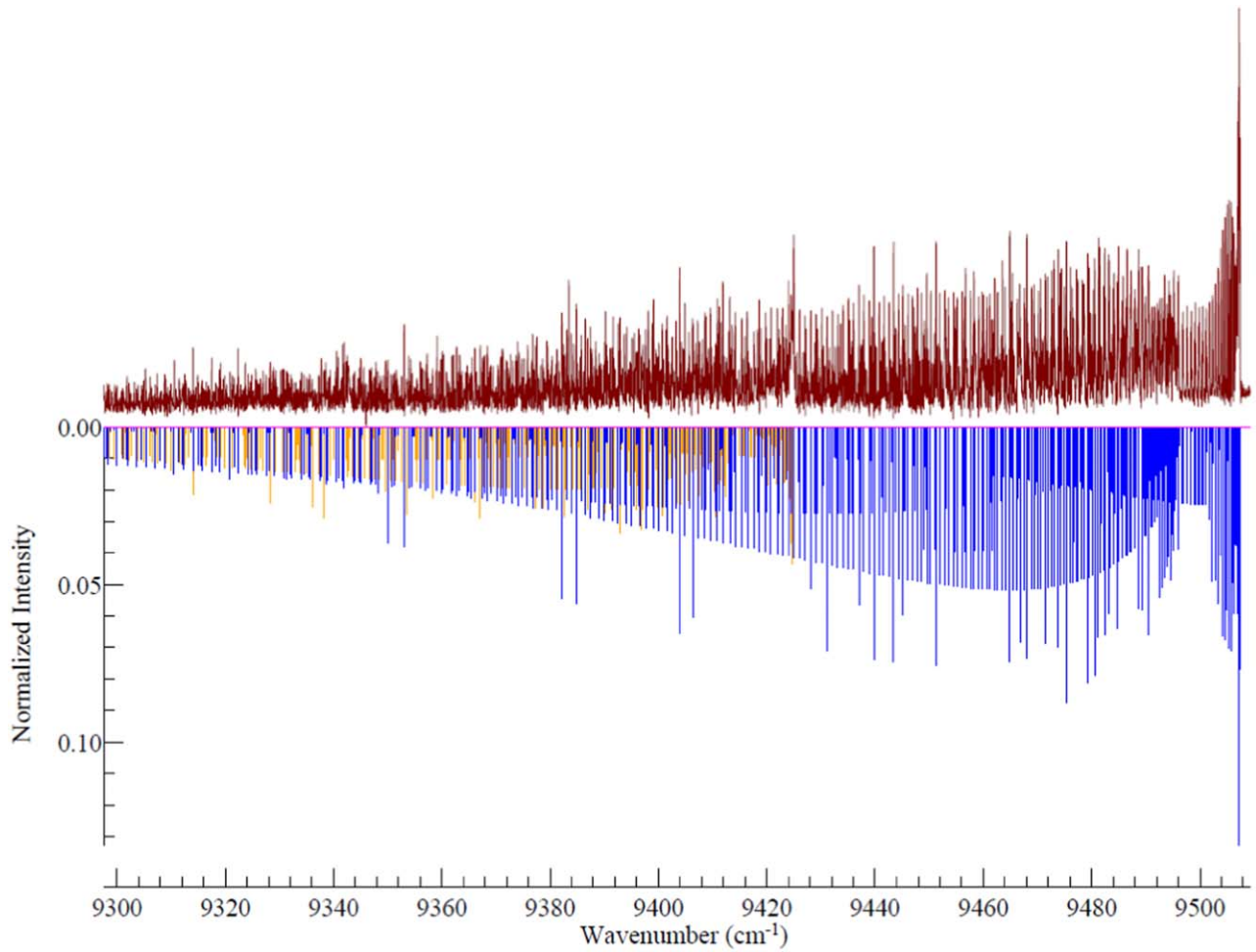
Figure 3. Typical $^{90}\text{Zr}^{16}\text{O}$ $B^1\Pi$–$A^1\Delta$ spectrum (red, upward) with a simulated R-branch head for the 0–0 band (blue, downward) and 1–1 band (yellow, downward)

Table 2
Sample of Lines and Residuals for the $^{90}\text{Zr}^{16}\text{O}$ $B^1\Pi$–$X^1\Sigma^+$, $B^1\Pi$–$A^1\Delta$, and $C^1\Sigma^+$–$X^1\Sigma^+$ Transitions from the PGOPHER Log File

J'	P'	J''	P''	Obs (cm^{-1})	Calc (cm^{-1})	O–C (cm^{-1})	Line Assignment
20	e	19	e	15,391.4090	15,391.3999	0.0091	R(19): B1Pi $v = 0$ 20e–X1Sigma $v = 0$ 19e
19	e	18	e	15,391.4090	15,391.4057	0.0033	R(18): B1Pi $v = 0$ 19e–X1Sigma $v = 0$ 18e
22	e	21	e	15,391.2802	15,391.2601	0.0201	R(21): B1Pi $v = 0$ 22e–X1Sigma $v = 0$ 21e
23	e	22	e	15,391.1434	15,391.1260	0.0174	R(22): B1Pi $v = 0$ 23e–X1Sigma $v = 0$ 22e
24	e	23	e	15,390.9681	15,390.9491	0.0190	R(23): B1Pi $v = 0$ 24e–X1Sigma $v = 0$ 23e
25	e	24	e	15,390.7479	15,390.7294	0.0185	R(24): B1Pi $v = 0$ 25e–X1Sigma $v = 0$ 24e
16	e	17	e	9477.9757	9477.9733	0.0024	Pe(17): B1Pi $v = 0$ 16e–A1Delta $v = 0$ 17e
16	f	17	f	9478.0361	9478.0377	−0.0015	Pf(17): B1Pi $v = 0$ 16f–A1Delta $v = 0$ 17f
58	e	58	f	9444.4061	9444.4046	0.0015	Qf(58): B1Pi $v = 0$ 58e–A1Delta $v = 0$ 58f
37	f	38	f	9443.7537	9443.753	0.0007	Pf(38): B1Pi $v = 0$ 37f–A 1Delta $v = 0$ 38f
91	e	90	e	16,975.4809	16,975.467	0.0139	R(90): C1Sigma $v = 0$ 91e–X1sigma $v = 0$ 90e
50	e	51	e	16,961.8936	16,961.8988	−0.0052	P(51): C1Sigma $v = 0$ 50e–X1sigma $v = 0$ 51e
88	e	87	e	16,982.8763	16,982.8702	0.0061	R(87): C1Sigma $v = 0$ 88e–X1sigma $v = 0$ 87e
73	e	72	e	17,014.705	17,014.7042	0.0008	R(72): C1Sigma $v = 0$ 73e–X1sigma $v = 0$ 72e

Note. J is total angular momentum, P is the e/f parity, Obs is the observed line position in cm^{-1}, Calc is the calculated line position in cm^{-1}, and $O-C$ is the observed minus calculated line position in cm^{-1}.

(This table is available in its entirety in machine-readable form.)

error of 0.015 cm^{-1}. Table 1 shows the calculated $^{90}\text{Zr}^{16}\text{O}$ R bandheads, 19 of which have been previously reported (Phillips & Davis 1976a; Sorensen & Bernath 2021) and two of which are new (bold values). Table 2 provides the observed line positions,

and Tables 3 and 4 the spectroscopic constants obtained from the PGOPHER fit for the $X^1\Sigma^+$ and $B^1\Pi$ states.

For the $B^1\Pi$–$A^1\Delta$ transition the fit included 2790 lines associated with the 0–0, 0–1, 1–0, 1–1, and 2–1 bands with an
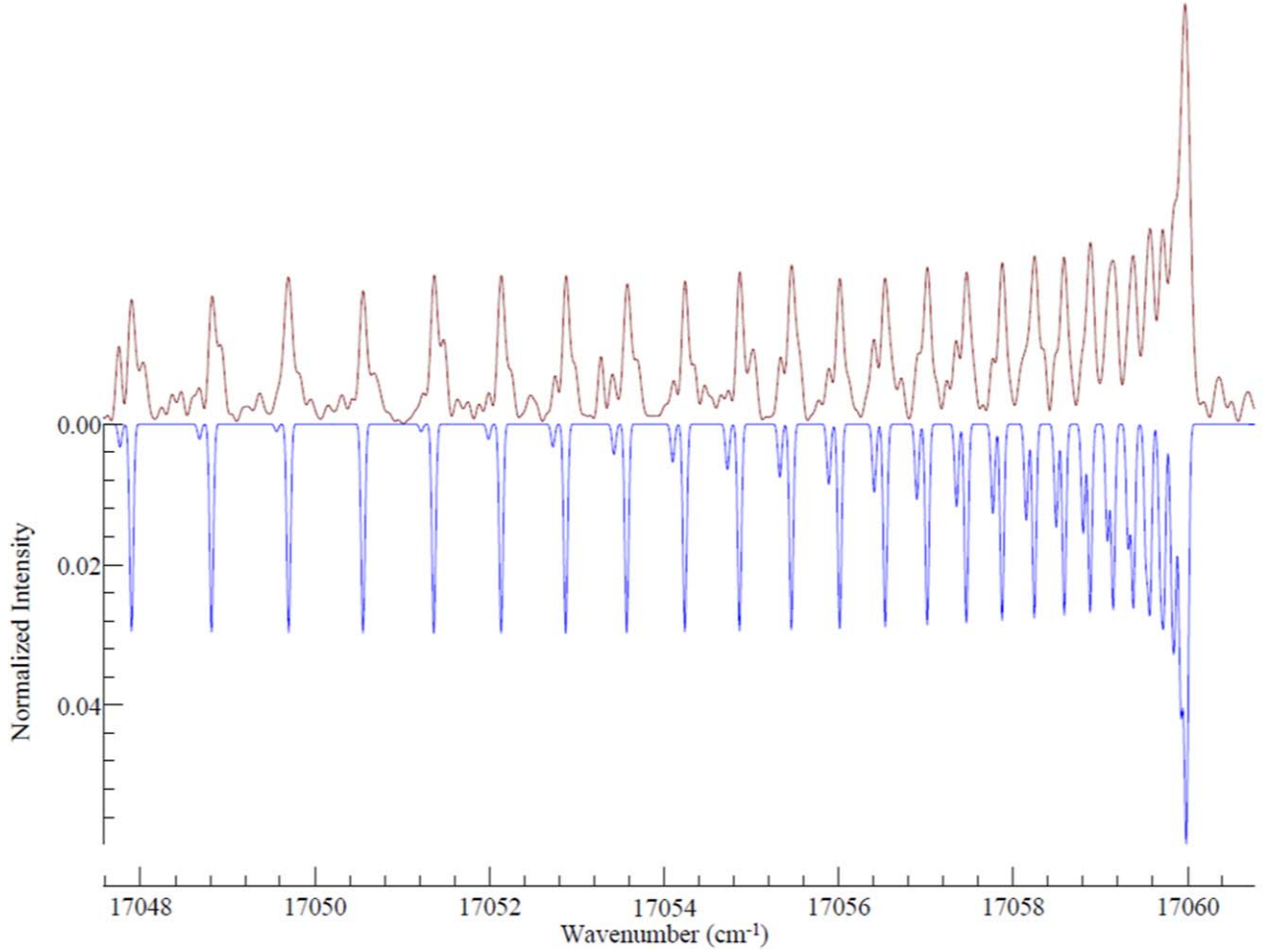
Figure 4. ^{90}Zr^{16}O $C^1\Sigma^+$–$X^1\Sigma^+$ spectrum (red, upward) with a simulated R-branch head for the 0–0 band (blue, downward)

Table 3
^{90}Zr^{16}O Spectroscopic Constants (in cm^{-1}) of the $X^1\Sigma^+$ State for $v = 0 - 7$ with a 1 Standard Deviation Error Indicated in Parentheses as Obtained from PGOPHER

v	T_v	B_v	$D_v \times 10^7$	$H_v \times 10^{13}$
0	0	0.42261086(554)	3.17714(542)	−0.50(15)
1	969.5271(16)	0.42066068(546)	3.20005(527)	0.77(14)
2	1932.1582(16)	0.41871098(550)	3.23480(533)	2.492(146)
3	2887.9104(17)	0.41674871(551)	3.26186(536)	3.824(147)
4	3836.7706(21)	0.41477259(553)	3.26593(544)	3.300(152)
5	4778.7271(19)	0.41279389(555)	3.29429(552)	4.984(159)
6	5713.7565(24)	0.41081684(564)	3.33218(578)	6.767(178)
7	6641.8924(26)	0.40880945(581)	3.32195(664)	6.232(264)

average error of 0.015 cm^{-1}. The $A^1\Delta$ $v = 0$ and 1 spectroscopic constants are reported in Table 5.

The $v = 0$ level of the $C^1\Sigma^+$ state is perturbed by the $v = 2$ level of the $B^1\Pi$ state (Phillips & Davis 1976b). The $v = 0$ $C^1\Sigma^+$ level crosses the $v = 2$ $B^1\Pi$ level at about $J' = 68$. So, we fitted 456 lines associated with the 0–0 band of the $C^1\Sigma^+$–$X^1\Sigma^+$ transition and the 2–0 band of the $B^1\Pi$–$X^1\Sigma^+$ transition together using the symmetrized matrix element $\langle A, v = 2|2J^+L^-|C, v = 0\rangle = 2\sqrt{J(J + 1)/2}$. The average error in the fit was 0.018 cm^{-1} and the $C^1\Sigma^+$ spectroscopic constants are reported in Table 6. The $B^1\Pi$–$A^1\Delta$ and $C^1\Sigma^+$–$X^1\Sigma^+$ fits fixed the ground $X^1\Sigma^+$ and the $B^1\Pi$ constants to the values in Tables 3 and 4. The fitted lines are provided as

supplemental data. Our line positions go to higher J values than the Simard et al. (1988) analysis based on laser-excitation spectra of a jet-cooled laser vaporization source. The line positions of Phillips & Davis (1976b) go to high J values but are not as accurate as our new values because they are from an arc source recorded with a grating spectrograph.

The spectroscopic constants obtained through the spectral line fit for ^{90}Zr^{16}O, as shown in Tables 3 and 4, are used to obtain the equilibrium constants ω_e, $\omega_e x_e$, $\omega_e y_e$, B_e, α_e, γ_e, δ_e, D_e, and β_e, Equations (1)–(3) below are for the excited $B^1\Pi$ and ground $X^1\Sigma^+$ states of ^{90}Zr^{16}O as shown in Table 7 along with previously reported values. Table 8 also contains equilibrium constants for the $A^1\Delta$ state, although data for only $v = 0$ and 1 were obtained. To estimate ω_e and $\omega_e x_e$, $\omega_e x_e = 3.1912$ cm^{-1} (Hammer & Davis 1981) was combined with $\Delta G_{1/2} = 935.92$ cm^{-1} (Table 8) to give $\omega_e = 942.305$ cm^{-1}. For the $C^1\Sigma^+$ state, data for only $v = 0$ was measured so $\omega_e = 876$ cm^{-1}, $\omega_e x_e = 3$ cm^{-1}, and $\alpha_e = 0.00165$ cm^{-1} were taken from Simard et al. (1988) and combined with B_0 (Table 6) to give $B_e = 0.40563605$ cm^{-1}

$$G_v = \omega_e\left(v + \frac{1}{2}\right) - \omega_e x_e\left(v + \frac{1}{2}\right)^2 + \omega_e y_e\left(v + \frac{1}{2}\right)^3 + ... \quad (1)$$

$$B_v = B_e - \alpha_e\left(v + \frac{1}{2}\right) - \gamma_e\left(v + \frac{1}{2}\right)^2 + \delta_e\left(v + \frac{1}{2}\right)^3 + ... \quad (2)$$
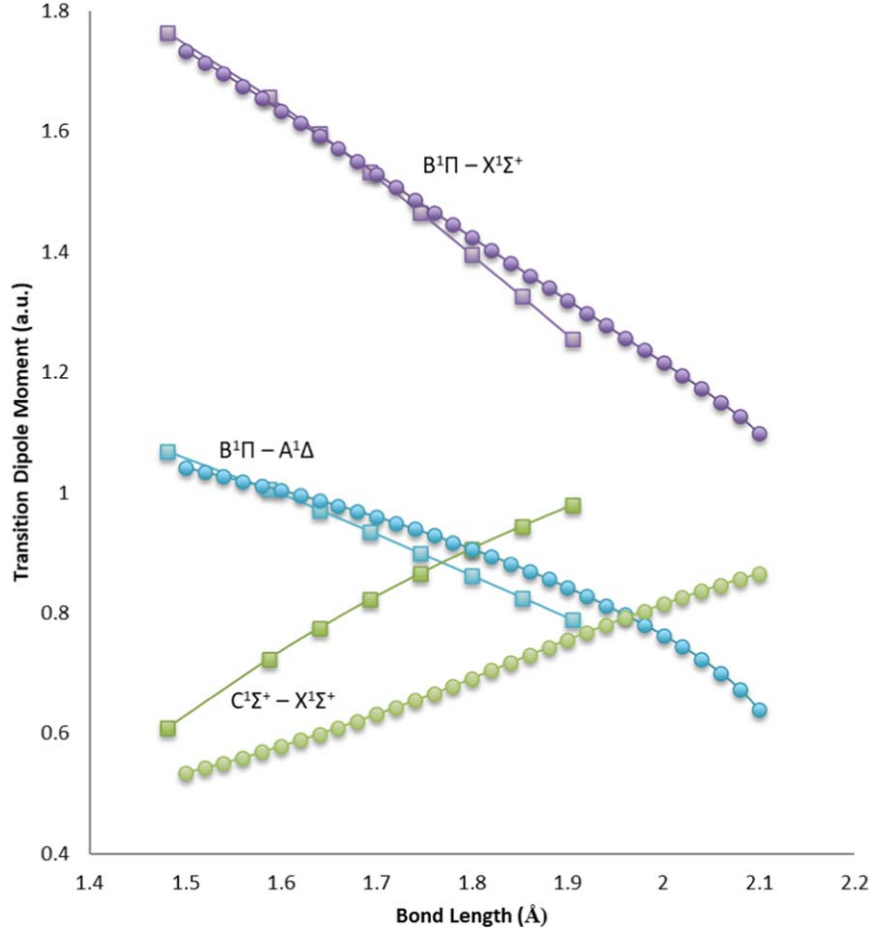
Figure 5. Computed transition dipole moment functions for the $B^1\Pi$–$X^1\Sigma^+$ (purple), $B^1\Pi$–$A^1\Delta$ (blue), and $C^1\Sigma^+$–$X^1\Sigma^+$ (green) transitions. Square markers indicate transition dipole moment data taken from Langhoff & Bauschlicher (1990), and circles represent transition dipole moments computed in this work. The y-axis is in atomic units, with 1 a.u. = 2.5417 debye.

(The data used to create this figure are available.)

Table 4
$^{90}Zr^{16}O$ Spectroscopic Constants (in cm^{-1}) of the $B^1\Pi$ State for $v = 0 - 5$ in with a 1 Standard Deviation Error Indicated in Parentheses as Obtained from PGOPHER

v	T_v	B_v	$D_v \times 10^7$	$H_v \times 10^{13}$	$q_v \times 10^4$	$q_{D_v} \times 10^9$
0	15,383.4208(13)	0.40151627(549)	3.50636(532)	−0.28(14)	−2.3673(28)	1.041(14)
1	16,236.9632(14)	0.39961155(551)	3.55471(535)	2.767(147)	−2.3291(37)	8.74(24)
2	17,084.6130(14)	0.39768122(550)	3.56869(534)	3.265(147)	−2.3055(33)	0.819(24)
3	17,926.2955(19)	0.39574427(552)	3.58941(542)	4.401(152)	−2.3718(41)	1.982(35)
4	18,762.0048(19)	0.39379547(556)	3.61338(555)	5.974(162)	−2.2993(48)	1.618(46)
5	19,591.6863(25)	0.39182947(578)	3.62373(657)	7.383(261)	−2.3174(80)	2.594(87)

Table 5
$^{90}Zr^{16}O$ Spectroscopic Constants for the $A^1\Delta$ State for $v = 0$ and 1 in cm^{-1}

v	T_v	B_v	$D_v \times 10^7$	$H_v \times 10^{13}$
0	5887.19588(93)	0.41645893(52)	3.26039(69)	−3.96(24)
1	6823.11895(88)	0.41459260(65)	3.3202(11)	3.338(54)

$$D_v = D_e - \beta_e\left(v + \frac{1}{2}\right). \quad (3)$$

After completing these spectroscopic fits and computations, our attention turned to producing line lists that included line strengths.

Table 6
$^{90}Zr^{16}O$ Spectroscopic Constants for the $C^1\Sigma^+$ State for $v = 0$ in cm^{-1}

T_0	B_0	$D_0 \times 10^7$
17,050.4060(24)	0.40480978(97)	3.45068(73)

Note. Perturbation term 0.004065(54) $\langle A, v = 2|2J^+L^-|C, v = 0\rangle$ is added to the Hamiltonian.

This was achieved by utilizing Le Roy's RKR and LEVEL programs (Le Roy 2017a, 2017b). The RKR program utilizes the first-order semiclassical Rydberg–Klein–Rees (RKR) method to approximate diatomic molecule potential energy surfaces. By

Table 7
Equilibrium Constants for the $B^1\Pi$ and $X^1\Sigma^+$ States in cm^{-1} or Å for r_e

Constants	$B^1\Pi$		$X^1\Sigma^+$	
	This Work	Previous Works	This Work	Previous Works
ω_e	859.4201(171)	859.424252(344)[a] 859.44[b]	976.3962(104)	976.40869(593)[a] 976.51[b]
$\omega_e x_e$	2.92554(665)	2.921697(161)[a] 2.918[b]	3.43556(303)	3.44153(116)[a] 3.462[b]
$\omega_e y_e \times 10^3$	−6.422(732)	−7.2866(212)[a] −8.12[b]	−1.169(249)	0.52[b]
B_e	0.40246814(390)	0.402460322(736)[a]	0.42357926(511)	0.4235669(134)[a]0.423608[b]
$\alpha_e \times 10^3$	1.89695(305)	1.8770(132)[a] 1.920[b]	1.93751(297)	1.9186(126)[a] 1.954[b]
$\gamma_e \times 10^6$	−6.790(494)	−26.11(618)[a] −5.0[b]	−4.175(361)	−10.68(246)[a] −3.3[b]
$D_e \times 10^7$	3.5089(86)	3.52[b]	3.1726(83)	3.19[b]
$\beta_e \times 10^9$	2.24(25)	...	2.21(18)	...
r_e	1.75629524(851)	1.75631230(44)[a] 1.75831(13)[c]	1.71196914(103)	1.71199404(79)[a] 1.71195242(73)[d] 1.71387(13)[c]

Notes.
[a] Sorensen & Bernath (2021).
[b] Phillips & Davis (1976a) Phillips and Davis did not report error limits on their values.
[c] Pettersson et al. (2000).
[d] Beaton & Gerry (1999).

Table 8
Equilibrium Constants for the $A^1\Delta$ State in cm^{-1} or Å for r_e

	This Work	Previous Works
$\Delta G_{1/2}$	935.92	935.9335[a]
B_e	0.417389	0.417392(10)[b]
$\alpha_e \times 10^3$	1.866	1.866(10)[b]
r_e	1.724611	1.725(2)[c]

Notes. As we only fit the $v = 0$ and $v = 1$ states for the $A^1\Delta$ state, error analysis was not possible.
[a] This value is a $\Delta G_{1/2} = \omega_e - 2\omega_e x_e$.
[b] Hammer & Davis (1981).
[c] McKemmish et al. (2018).

knowing the vibrational quantum number (v) dependence of molecular vibrational energies, G_v, and the inertial rotational constants, B_v, the RKR method can determine these potential energy surfaces.

These RKR potential energy surfaces are then combined with our computed $B^1\Pi$–$X^1\Sigma^+$, $B^1\Pi$–$A^1\Delta$, and $C^1\Sigma^+$–$X^1\Sigma^+$ transition dipole moment functions, which are shown in Figure 5 (along with a comparison to the transition dipole moment functions reported by Langhoff & Bauschlicher 1990) as the input to the LEVEL program. The LEVEL program uses this input data to solve the one-dimensional Schrödinger equation to compute output parameters such as band strengths and Franck–Condon factors with the band strengths being shown in Table 9 for the $B^1\Pi$–$X^1\Sigma^+$ transition and Table 10 for the $B^1\Pi$–$A^1\Delta$ and $C^1\Sigma^+$–$X^1\Sigma^+$ transitions. These output band strengths were then entered into PGOPHER to determine the individual line strengths for the observed $B^1\Pi$–$X^1\Sigma^+$, $B^1\Pi$–$A^1\Delta$, and $C^1\Sigma^+$–$X^1\Sigma^+$ transitions. PGOPHER was utilized to output a line list of all possible $B^1\Pi$–$X^1\Sigma^+$ bands with $v' \leqslant 5$ and $v'' \leqslant 7$, $B^1\Pi$–$A^1\Delta$ with $v' \leqslant 2$ and $v'' \leqslant 1$ and $C^1\Sigma^+$–$X^1\Sigma^+$ with $v' = v'' = 0$ for ^{90}Zr^{16}O. These line lists are provided for all possible bands up to $J = 200$ as .csv files as an extended table with a table stub displayed in Table 11. Note that for J values greater than the highest experimentally observed values, the predicted line positions start to deviate from their true values. However, they are still useful because they provide opacity for the simulation of astronomical spectra.

5. Discussion

The spectroscopic constants listed in Tables 4 and 5 were derived from the spectroscopic fit of the lines listed in Table 2 ($B^1\Pi$–$X^1\Sigma^+$ transition) and similar fitted lines for the $B^1\Pi$–$A^1\Delta$ and $C^1\Sigma^+$–$X^1\Sigma^+$ transitions. For the $C^1\Sigma^+$–$X^1\Sigma^+$ transition, this study represents the first high-resolution Fourier transform spectroscopic analysis of ^{90}Zr^{16}O. In the case of the $B^1\Pi$–$X^1\Sigma^+$ transition, this work represents an improvement over previous studies as the spectrum used had a higher S/N, which enabled us to extend the number of observed ^{90}Zr^{16}O bands from 19–21 (see Table 1).

The theoretical equilibrium spectroscopic properties determined from our MRCI+Q potential energy curves are compared in Table 12 to our experimental values and to previous ab initio calculations (Langhoff & Bauschlicher 1990; Tabet et al. 2019). These latter works adopted a similar MRCI approach to ours, but with smaller basis sets and active spaces, and without taking the correlation energy arising from the zirconium 4s4p shell into account. As can be noted, this contribution reinforces the molecular bonding (smaller r_e and larger ω_e values), and significantly improves the agreement with the experimental values. The mean absolute deviations of our calculations are 0.003 Å and 5 cm^{-1} for r_e and ω_e, respectively, while those of Langhoff & Bauschlicher (1990) are 0.021 Å and 15 cm^{-1}, and those of Tabet et al. (2019) are 0.027 Å and 20 cm^{-1}. B_e and α_e are also calculated with a reasonable accuracy of 10^{-3} and 8×10^{-5} cm^{-1}, respectively. The term energies T_e are predicted within 200–700 cm^{-1} from the corresponding experimentally derived values, depending on the considered transition, with similar deviations for the previous calculations.

The transition dipole moment functions for the $B^1\Pi$–$X^1\Sigma^+$, $B^1\Pi$–$A^1\Delta$, and $C^1\Sigma^+$–$X^1\Sigma^+$ transitions are shown in Figure 5, along with a comparison to the transition dipole moment functions reported by Langhoff & Bauschlicher (1990). Both calculations globally agree for the first two transitions, while our functions have a smaller slope and the curvature is more pronounced in the case of the $B^1\Pi$–$A^1\Delta$ transition. The discrepancy is greater for the $C^1\Sigma^+$–$X^1\Sigma^+$ transition, for which we obtain lower values of 0.1–0.2 a.u. (atomic units). This difference probably comes from competing differential effects in which the 4p4d correlation should play a role.

Table 9
Band Strengths $\langle v'J'|M|v''J''\rangle$ (debye) for the $^{90}Zr^{16}O$ $B^1\Pi$–$X^1\Sigma^+$ Transition from the LEVEL Program

v'/v''	0	1	2	3	4	5	6	7
0	3.15858	1.82313	0.736997	0.233988	0.0604626	0.0125252	0.00155426	−0.000442749
1	−1.97628	1.99399	2.10723	1.12731	0.428718	0.124876	0.0260497	0.000844962
2	0.896335	−2.26374	1.04133	2.07071	1.40108	0.617556	0.193181	0.0343972
3	−0.335726	1.35763	−2.19513	0.280239	1.87803	1.58401	0.786599	0.247639
4	0.108279	−0.612764	1.66367	−1.94396	−0.305388	1.61581	1.69877	0.921369
5	−0.0303094	0.229122	−0.879521	1.83918	−1.58416	−0.727277	1.34260	1.76681

Table 10
Band Strengths $\langle v'J'|M|v''J''\rangle$ (debye) for the $^{90}Zr^{16}O$ $B^1\Pi$–$A^1\Delta$, and $C^1\Sigma^+$–$X^1\Sigma^+$ Transitions from the LEVEL Program

	v'/v''	0	1
$B^1\Pi$–$A^1\Delta$	0	2.17295E	0.884939
	1	−0.972823	1.76009
$C^1\Sigma^+$–$X^1\Sigma^+$	0	1.45395	...
	2	0.314755	−1.24506

Table 11
Sample Table for the PGOPHER Line List for the $^{90}Zr^{16}O$, $B^1\Pi$–$X^1\Sigma^+$, $B^1\Pi$–$A^1\Delta$, and $C^1\Sigma^+$–$X^1\Sigma^+$ Transitions

J'	J''	Pos (cm^{-1})	E_{up}(cm^{-1})	E_{low}(cm^{-1})	A(s^{-1})	$f \times 10^3$	Line Assignment
65	65	16,977.4610	18,784.6104	1807.1494	1,232,994	6.41	:Q(65) :B1Pi $v=2$ 65f–X1Sigma $v=0$ 65e
50	51	16,977.5652	18,096.0938	1118.5286	61,0404.5	3.11	:P(51) :B1Pi $v=2$ 50e–X1Sigma $v=0$ 51e
83	82	16,977.6697	19,839.2264	2861.5568	620,211.7	3.26	:R(82) :B1Pi $v=2$ 83e–X1Sigma $v=0$ 82e
157	157	16,978.3149	29,101.7723	12,123.4574	1,187,349	6.18	:Q(157) :B1Pi $v=5$ 157f–X1Sigma $v=2$ 157e
157	158	16,978.2952	28,314.9151	11,336.6198	28,7250	1.48	:P(158) :B1Pi $v=4$ 157e–X1Sigma $v=1$ 158e
64	64	16,980.7277	18,733.2870	1752.5594	1,233,706	6.41	:Q(64) :B1Pi $v=2$ 64f–X1Sigma $v=0$ 64e
98	97	11,232.8124	21,731.3643	10,498.5519	13,698.56	0.164	:R(97) :B1pi $v=3$ 98e–X1Sigma $v=7$ 97e
67	66	8554.9356	17,204.9196	8649.984	36,466.81	0.758	:Re(66) : B1Pi $v=0$ 67e–A1Delta $v=1$ 66e
69	68	8554.0082	17,315.1208	8761.1126	36,511.33	0.759	:Rf(68) : B1i $v=0$ 69f–A1Delta $v=1$ 68f
15	15	8557.1341	15,479.7361	6922.6021	76304.4	1.56	Qf(15) : B1Pi $v=0$ 15e–A1Delta $v=1$ 15f
10	11	17,039.152	17,094.9308	55.7788	87,6167.7	4.13	:P(11) : C1Sigma $v=0$ 10e–X1sigma $v=0$ 11e
13	14	17,035.336	17,124.0697	88.7338	866,732.9	4.17	: P(14) : C1Sigma $v=0$ 13e–X1sigma $v=0$ 14e
139	138	16,808.0964	24,797.336	7989.2396	799,860.1	4.28	:P(138) : C1Sigma $v=0$ 139e–X1Sigma $v=0$ 138e
143	142	16,789.8506	25,239.9356	8450.085	797,341.8	4.27	:P(142) : C1Sigma $v=0$ 143e–X1sigma $v=0$ 142e

Note. J is the total angular momentum, Pos is the calculated line position in cm^{-1}, E_{up} and E_{low} are the upper and lower energy levels in cm^{-1}, A is the Einstein $A_{J'\leftarrow J''}$ value in s^{-1}, and $A_{J'\leftarrow J''}$ is the oscillator strength, and line assignments are the associated quantum numbers for the given transition.

(This table is available in its entirety in machine-readable form.)

Tables 7 and 8 provide the derived equilibrium molecular constants for the $X^1\Sigma^+$, $B^1\Pi$, and $A^1\Delta$ states of $^{90}Zr^{16}O$ along with previously reported values. We note that some of the previous values come from the work of Phillips & Davis (1976a) for which no error limits were reported. Attempts were made to fit higher order terms such as $\omega_e z_e$ ($X^1\Sigma^+$ and $B^1\Pi$ state) and δ_e ($X^1\Sigma^+$ state); however, the errors were too large for confidence. Equilibrium bond lengths, r_e in Å, are also presented in Tables 7 and 8 and were calculated from the equilibrium rotational constant, B_e in cm^{-1} using the standard equation (Bernath 2020). The reduced mass of $^{90}Zr^{16}O$ was calculated using atomic masses taken from the new atomic mass evaluation, AME2020 (Wang et al. 2021). The line lists provided in this work (as sampled in Table 11) contain both the Einstein $A_{J'\rightarrow J''}$ values and oscillator strengths $f_{J'\leftarrow J''}$ in which the Einstein A coefficients were converted into oscillator

strengths (Bernath 2020) using

$$f_{J'\leftarrow J''} = \frac{1.499194}{\tilde{\nu}^2}\frac{2J'+1}{2J''+1}A_{J'\rightarrow J''} \qquad (4)$$

with $\tilde{\nu}$ in cm^{-1}.

An estimate of the error of our reported line strengths can be made by comparing our computed radiative lifetimes, τ, to known experimental radiative lifetimes. Table 13 gives the computed radiative lifetimes for the $^{90}Zr^{16}O$ $B^1\Pi$ $v=0$, 1, 2, 3, 4 levels. These lifetimes include transitions from the $B^1\Pi$ state to both the $A^1\Delta$ and $X^1\Sigma^+$ states. Also included in Table 13 are radiative lifetimes from our previous work on the $B^1\Pi$–$X^1\Sigma^+$ transition along with experimental values obtained from laser-induced fluorescence measurements of supersonically cooled ZrO (Simard et al. 1988). The radiative lifetimes were computed by taking the band strengths from the LEVEL

Table 12
Equilibrium Spectroscopic Constants for the $X^1\Sigma^+$, $A^1\Delta$, $B^1\Pi$, and $C^1\Sigma^+$ States of ZrO from Ab Initio Calculations (in cm^{-1} and Å for r_e)

		r_e	B_e	$\alpha_e \times 10^3$	ω_e	$\omega_e x_e$	T_e
$X^1\Sigma^+$	calc.[a]	1.7136	0.42276	1.933	982.4	3.35	0
	calc.[b]	1.734	...	...	941.5	...	0
	calc.[c]	1.74	...	...	965	2.8	0
	exp.[d]	1.71197	0.42358	1.9375	976.396	3.435	0
$A^1\Delta$	calc.[a]	1.7289	0.41533	1.839	943.4	3.06	5725
	calc.[b]	1.747	...	...	920.4	...	5230
	calc.[c]	1.75	...	...	932	2.9	6302
	exp.[d]	1.72461	0.41739	1.87	942.305	3.19[e]	5907.37[f]
$B^1\Pi$	calc.[a]	1.7515	0.40467	2.070	865.003	3.08	15,935
	calc.[b]	1.774	...	...	857.5	...	15048
	calc.[c]	1.78	...	...	855	2.4	15,575
	exp.[d]	1.75630	0.40247	1.8970	859.4	2.92	15,441.78[f]
$C^1\Sigma^+$	calc.[a]	1.7502	0.40528	1.750	883.1	2.00	17,675
	calc.[b]	1.772	...	...	873.2	...	17,278
	calc.[c]	1.78	...	...	867	2.8	18,219
	exp.[d]	1.74942	0.40564	1.65[g]	876[g]	3[g]	17,100.50[f]

Notes. Comparison with experimental and previous theoretical work.
[a] This work.
[b] Langhoff & Bauschlicher (1990).
[c] Tabet et al. (2019).
[d] This work (see the text, Tables 7 and 8) or otherwise specified.
[e] Hammer & Davis (1981).
[f] Derived from available experimental T_0, ω_e, $\omega_e x_e$, and $\omega_e y_e$ values.
[g] Simard et al. (1988).

program (Tables 9 and 10) and converting them into Einstein A values (Bernath 2020), which then can be converted into lifetimes τ, using $\tau_{v'} = 1/\sum_{v''} A_{v' \to v''}$. The average error between our lifetimes and those of Simard et al. (1988) is about 25%, which is our error estimate.

Plez et al. (2003) compiled line lists for a number of ZrO electronic transitions. A comparison between our PGOPHER energy levels and those of Plez et al. (2003) for the $B^1\Pi$ and $X^1\Sigma^+$ states agree to within about 0.1 cm^{-1} for $J <$ 60; however, the levels deviate rapidly for high J values with deviations on the order of 5–10 cm^{-1}. Similar deviations are also observed for the $A^1\Delta$ and $C^1\Sigma^+$ states, although with fewer vibrational levels for comparison. As expected, however, our energy levels for the $X^1\Sigma^+$, $B^1\Pi$, $A^1\Delta$, and $C^1\Sigma^+$ states agree to better than 0.2 cm^{-1} up to about $J = 120$ with MARVEL energy levels (McKemmish et al. 2018). These MARVEL energy levels were derived from older ZrO experimental data.

The spectra of ZrO are dominated by ^{90}ZrO with a 51.5% natural abundance, but the four minor isotopologue abundances are not negligible (^{91}ZrO 11.2%, ^{92}ZrO 17.2%, ^{94}ZrO 17.4%, ^{96}ZrO 2.8%; Rumble 2022). The line positions (or isotopic shifts) of the minor isotopologues can be calculated from the spectroscopic constants provided in Tables 3–8 using the usual isotopic relationships (Bernath 2020), for example, as was recently carried out for TiO (Bernath & Cameron 2023). The line strengths for the minor isotopologues are approximately the same as for the ^{90}ZrO; however, their band strengths can also be calculated with the LEVEL program by changing the isotopic mass.

After our paper was submitted, a comprehensive line list for ZrO (including isotopologues) was published by Perri et al. (2023). Their line positions for the B–X transition are based on our previous analysis and on the literature values for the B–A and C–X transitions. Although our new line positions

Table 13
Comparison of ^{90}Zr^{16}O $B^1\Pi$ ($v = 0, 1, 2, 3, 4$) Radiative Lifetimes, τ (in ns)

v'	This Work	Previous Work[a]	Experiment[b]	Theory[c]
0	61.03	68.5	83	56.4
1	62.65	69.2	83	...
2	65.56	70.8	83	...
3	68.72	81.9	90	...
4	69.51	...	...	...

Notes. Simard et al. (1988) reported their lifetimes without error limits.
[a] Sorensen & Bernath (2021).
[b] Simard et al. (1988).
[c] Langhoff & Bauschlicher (1990).

improve on these values, the differences are typically less than 0.05 cm^{-1}. The Perri et al. (2023) Einstein A values, however, vary more and differ by about 10%–50% for the B–X transition presumably because of differences in the transition dipole moment functions. The Perri et al. (2023) calculations are similar to those of Tabet et al. (2019) (see Table 12) and our calculations use larger basis sets and correlate more electrons. It is likely (Table 12) that our transition dipole moment functions are more accurate.

6. Conclusion

High-resolution spectra of hot ZrO were reanalyzed in the near-IR and visible regions. Lines associated with 21 bands of the $B^1\Pi$–$X^1\Sigma^+$ transition, along with five bands of the $B^1\Pi$–$A^1\Delta$ transition and one band of the $C^1\Sigma^+$–$X^1\Sigma^+$ transition were observed and fit using PGOPHER. Updated spectroscopic constants are reported. In general, we improve the accuracy of the line positions reported in the literature and slightly extend the vibrational analysis. New ab initio

calculations of the transition dipole moment functions were performed and used to determine line strengths. New line lists for the $B^1\Pi$–$X^1\Sigma^+$, $B^1\Pi$–$A^1\Delta$, and $C^1\Sigma^+$–$X^1\Sigma^+$ transitions were calculated. These line lists are useful for accurate modeling and identification of S-type stars, although we note that the spectra of cool stars are very complicated with many overlapping lines from several molecules and atoms.

Acknowledgments

ORCID iDs

Peter F. Bernath ⓘ https://orcid.org/0000-0002-1255-396X
Manish Bhusal ⓘ https://orcid.org/0009-0008-6042-3271
Jacques Liévin ⓘ https://orcid.org/0000-0002-5557-7486

References

Ake, T. B. 1979, ApJ, 234, 538
Balfour, W. J., & Chowdhury, P. K. 2010, CPL, 485, 8
Balfour, W. J., & Tatum, J. B. 1973, JMoSp, 48, 313
Beaton, S. A., & Gerry, M. C. 1999, JChPh, 110, 10715
Bernath, P., & Cameron, D. 2023, JQSRT, 310, 108745
Bernath, P. F. 2020, Spectra of Atoms and Molecules (Oxford: Oxford Univ. Press)
Hammer, P. D., & Davis, S. P. 1981, ApJS, 47, 201
Hammer, P. D., Davis, S. P., & Zook, A. C. 1981, JChPh, 74, 5320
Keenan, P. C. 1954, ApJ, 120, 484
Keenan, P. C., & Boeshaar, P. C. 1980, ApJS, 43, 379
Kreplin, D. A., Knowles, P. J., & Werner, H.-J. 2019, JChPh, 150, 194106
Lambert, D. L., Smith, V. V., Busso, M., Gallino, R., & Straniero, O. 1995, ApJ, 450, 302
Langhoff, S. R., & Bauschlicher, C. W., Jr. 1988, JChPh, 89, 2160
Langhoff, S. R., & Bauschlicher, C. W., Jr. 1990, ApJ, 349, 369
Langhoff, S. R., & Davidson, E. R. 1974, IJQC, 8, 61
Lawler, J., Schmidt, J., & Den Hartog, E. 2022, JQSRT, 289, 108283
Le Roy, R. J. 2017a, JQSRT, 186, 158
Le Roy, R. J. 2017b, JQSRT, 186, 167
Li, X., Zheng, W., Buonaugurio, A., et al. 2012, JChPh, 136, 154306
Lowater, F. 1932, PPS, 44, 51
Lowater, F. 1935, RSPTA, 234, 355
Luo, Z., Chang, Y.-C., Zhang, Z., & Ng, C. 2015, MolPh, 113, 2228
McKemmish, L. K., Borsovszky, J., Goodhew, K. L., et al. 2018, ApJ, 867, 33
Merrill, P. W. 1922, ApJ, 56, 457
Merrill, P. W. 1923, PASP, 35, 217
Merrill, P. W. 1952, ApJ, 116, 21
Murad, E., & Hildenbrand, D. L. 1975, JChPh, 63, 1133
Perri, A. N., Taher, F., & McKemmish, L. K. 2023, MNRAS, 524, 4631
Peterson, K. A., Figgen, D., Dolg, M., & Stoll, H. 2007, JChPh, 126, 124101
Pettersson, A., Koivisto, R., Lindgren, B., et al. 2000, JMoSp, 200, 65
Phillips, J. G., & Davis, S. P. 1976a, ApJS, 32, 537
Phillips, J. G., & Davis, S. P. 1976b, ApJ, 206, 632
Plez, B., Van Eck, S., Jorissen, A., et al. 2003, in IAU Symp. 210, Modelling of Stellar Atmospheres, ed. N. Piskunov, W. W. Weiss, & D. F. Gray (San Francisco, CA: ASP)
Rumble, J. 2022, CRC Handbook of Chemistry and Physics (3rd ed.; Boca Raton, FL: CRC Press), 14
Simard, B., Mitchell, S., Humphries, M., & Hackett, P. 1988, JMoSp, 129, 186
Sorensen, J. J., & Bernath, P. F. 2021, ApJ, 923, 234
Suenram, R., Lovas, F., Fraser, G., & Matsumura, K. 1990, JChPh, 92, 4724
Tabet, J., Adem, Z., & Taher, F. 2019, Comput. Theor. Chem., 1160, 31
Tatum, J. B., & Balfour, W. J. 1973, JMoSp, 48, 292
Van Eck, S., & Jorissen, A. 1999, A&A, 345, 127
Van Eck, S., & Jorissen, A. 2000, A&A, 360, 196
Wang, M., Huang, W., Kondev, F. G., Audi, G., & Naimi, S. 2021, ChPhC, 45, 030003
Werner, H. J., Kállay, M., & Gauss, J. 2008, JChPh, 128, 034305
Werner, H. J., & Knowles, P. J. 1985, JChPh, 82, 5053
Werner, H. J., & Knowles, P. J. 1988, JChPh, 89, 5803
Werner, H.-J., Knowles, P. J., Knizia, G., Manby, F. R., & Schütz, M. 2012, WIREs: Computational Molecular Science, 2, 242
Werner, H.-J., Knowles, P. J., Knizia, G., et al. 2022 MOLPRO, a package of ab initio programs, https://www.molpro.net
Western, C. M. 2017, JQRST, 186, 221
Woon, D. E., & Dunning, T. H., Jr. 1993, JChPh, 98, 1358